ORIGINAL ARTICLE

Numerical simulation and PIV study of compressible vortex ring evolution

T. Murugan · S. De · C. L. Dora · D. Das

Abstract Formation and evolution of a compressible vortex ring generated at the open end of a short driver section shock tube has been simulated numerically for pressure ratios (PR) of 3 and 7 in the present study. Numerical study of compressible vortex rings is essential to understand the complicated flow structure and acoustic characteristics of many high Mach number impulsive jets where simultaneously velocity, density and pressure fields are needed. The flow development, incident shock formation, shock diffraction, vortex ring formation and its evolution are simulated using the AUSM+ scheme. The main focus of the present study is to evaluate the time resolved vorticity field of the vortex ring and the shock/expansion waves in the starting jet for short driver section shock tubes—a scenario where little data are available in existing literature. An embedded shock and a vortex induced shock are observed for PR = 7. However the vortex ring remains shock free, compact and unaffected by the trailing jet for PR = 3. Numerical shadowgraph shows the evolution of embedded shock and shock/expansion waves along with their interactions. The velocity and vorticity fields obtained from simulation are validated with the particle image velocimetry results and these data match closely. The translational velocity of the vortex ring, velocity across the vortex and the centre line velocity of the jet obtained from simulation also agree well with the experimental results.

Communicated by M. Brouillette.

T. Murugan (✉) · S. De
Central Mechanical Engineering Research Institute (CSIR),
Durgapur 713209, WB, India
e-mail: murugan.thangadurai@gmail.com

C. L. Dora · D. Das
Department of Aerospace Engineering, IIT, Kanpur 208016, UP, India

List of symbols

M	Mach number of the incident shock
U_b	Velocity behind the incident shock
U_r	Vortex ring translational velocity
u, v	x, y component of velocities
t	Time; $t = 0$ represents incident shock at shock tube exit
D	Inner diameter of the shock tube
PR	Pressure ratio between the driver and driven section
V_s	Shock speed
a	Local speed of sound

1 Introduction

Formation and evolution of a compressible vortex ring from the open end of a shock tube is a fascinating phenomenon which includes shock diffraction, boundary separation (slip stream), expansion of under expanded jet, formation of shock/expansion waves, and vortex sheet roll up. The dynamics of planar shock wave undergoing sudden expansion at the exit has been studied experimentally and numerically by many researchers [1–4] and they have addressed the effect of viscous dissipation on planar shock wave, the time accurate shock and vortex locations. Though the vortex sheet rollup and vortex ring formation are similar in impulsive flow from the orifice, nozzle [5–8] and shock tube exit, the flow field of vortex ring generated from shock tubes is complex due to diffraction of incident shock, expansion of flow and the

emergence of shock/expansion waves besides high vorticity levels and turbulence.

The study on compressible vortex rings emerging from shock tubes was initiated in 1952 by Elder and Hass [9]. They found the trajectory of vortex ring and incident shock using spark schlieren technique for small incident shock Mach number, $M = 1.12$ and 1.32. Phan and Stollery [10] observed an embedded shock within the vortex ring for $M = 1.5$ using schlieren photographs while engaged in noise suppression study. Baird [11] re-examined the problem and confirmed the presence of embedded shock from pressure measurements along the axis and flow visualization using differential interferometry. Brouillette and Hebert [12] characterized the flow field of compressible vortex rings for M varying from 1 to 2 using spark shadowgraphs. For $M = 1$–1.43, they observed conventional vortex rings with thin vortex core. The axial flow in the recirculating region of the vortex ring became supersonic and produced a rearward facing embedded shock for $M = 1.43$–1.6. A secondary counter rotating vortex ring (CRVR) ahead of the main vortex ring was observed for $M = 1.6$ to 2.

The quantitative experimental study of compressible vortex rings using particle image velocimetry (PIV) was initiated by Arakeri et al. [13] for $M = 1.1$, 1.2, and 1.3. The authors reported the velocity and vorticity fields of compressible vortex rings for $M = 1.2$. The vortex ring formation was found to be complete at a nondimensional time (tU_b/D) value of 2 and the translational velocity of vortex ring reached 0.7 U_b by the end of vortex ring formation. Murugan and Das [14–17] studied the effect of driver section lengths and M on the formation, evolution and interaction of circular vortex loops using qualitative flow visualizations and acoustic pressure measurements. They distinguished the noise generated by vortex rollup, trailing jet interaction and pinch off besides the shock and wall interaction noise from the microphone signal. They observed strong pressure fluctuations during the embedded shock and counter rotating vortex ring formations. Murugan and Das [18,19] also observed the complete evolution of CRVR and discussed the mechanism of CRVR formation and evolution. The translational velocity of the vortex loop was found to reduce significantly and the diameter increased noticeably during the CRVR formation.

Kontis et al. [20,21] studied the interaction of compressible vortex rings with various body shapes for PR = 4, 8, 12 using schlieren photography using long driver section circular shock tube. Their main finding was the formation of a series of secondary vortex rings ahead of primary vortex ring for PR = 12. According to the authors, the generation of the secondary vortex rings depended on the compressibility of the main vortex ring. Effect of elliptical, square and eye shaped nozzles on the generated vortex loops was investigated by Kontis et al. [22–25] for PR = 4, 8 and 12 using schlieren, shadowgraphy and PIV. The expansion of

the flow was dramatically decreased for eye shaped nozzle. Though the PIV results showed the velocity fields of primary, secondary and instability vortices, the presence of embedded shock and shock cell structure could not be distinguished in the quantitative results from PIV.

Acoustic characteristics of starting jet and subsequent vortex loop development are essential in pulse detonation engines [26], launch vehicles and many micro jets studies. The complete unsteady velocity and vorticity fields along with density and temperature fields are essential for understanding the acoustic fluctuations produced during vortex loop formation and evolution. However, such data cannot be extracted from experiments alone. Kontis et al. [25] also pointed out that quantitative data for the compressible vortex core are difficult to obtain from PIV for high magnitudes of vorticity. Though the velocity and vorticity fields of compressible vortex rings can be calculated quite reasonably from PIV measurements for high M, the shock cell structure, embedded shock and the vortex core are difficult to resolve. The accumulation of large number of particles behind the shock and at the vortex core causes dispersion in PIV results. Moreover, measuring the acoustic fluctuations generated during vortex ring formation and evolution experimentally is too difficult due to diffraction, interaction and reflection of incident shock [18].

All the aforesaid issues can be resolved by the development of an efficient and accurate numerical tool which is capable of producing simultaneous pressure, temperature and velocity field data. To make it reliable, the developed numerical solver has to be validated with the experimental results so that it can be used for other cases to study every aspect of compressible vortex ring. There are numerical simulations in the literature for flow inside shock tubes and impulsive flow from shock tubes. These are for some specific cases. Brun and Reboh [27] studied the flow inside the shock tube where perturbed flow patterns generated by the incident shock wave is modeled. Mirels [28,29] modeled the laminar boundary layer behind the shock advancing into stationary fluid. Petersen [30] proposed an improved turbulent boundary-layer model for shock tubes.

Flow field of a pulsatile jet from an exhaust pipe is studied experimentally and numerically by Endo and Iwamoto [31] where the flow inside the tube is simulated using random-choice method (RCM) under 1-D flow assumption. Saito and Takayama [32] studied the flow starting from the divergent nozzle placed at the shock tube exit by solving the Navier–Stokes equations using the Harten–Yee TVD scheme. The agreement between numerical and experimental results was good until the boundary layers became turbulent. Ishii et al. [33] studied the evolution of circular pulse jet using axisymmetric Euler equations with a finite difference TVD scheme for a wide range of jet strength. They found that the vortex ring near the exit plays a dominant role on

the formation of shock cell structure. They also noted that the K-H instability along the slip surface originating from the triple point at the Mach disk is responsible for the generation of secondary vortices. However the secondary vortices are affected significantly by viscosity and hence Euler equations are inadequate for capturing them.

In the present study, an attempt has been made to simulate the flow inside the short driver section shock tube and the resulting compressible vortex ring for obtaining the simultaneous velocity, pressure, and density field by solving the axisymmetric form of the Navier–Stokes equations. Short driver section shock tube of 165 mm length is used in the present work to minimize the unsteady effects of trailing jet on the evolution of compressible vortex ring. Two pressure ratios (PR) of 3 and 7 are selected in distinct flow regimes of vortex rings. Finally, the results obtained from simulation are verified with particle image velocimetry (PIV) results.

2 Governing equations and computational procedure

Impulsive flow generated from the open end of a shock tube is simulated by solving the axisymmetric equations of continuity, momentum and energy along with the equation of state in nondimensional form. Velocity is nondimensionalized as

$$u = \frac{\tilde{u}}{U_{\text{ref}}}, \quad \text{where } U_{\text{ref}} = k_0 a = k_0 \sqrt{\gamma R T_{\text{ref}}}$$

Density $\rho = \dfrac{\tilde{\rho}}{\rho_{\text{ref}}}$; Temperature $T = \dfrac{\tilde{T}}{T_{\text{ref}}}$

Pressure $p = \dfrac{\tilde{p}}{\rho_{\text{ref}} U_{\text{ref}}^2}$ where $\tilde{p} = \tilde{\rho} R \tilde{T} = \rho \rho_{\text{ref}} R T T_{\text{ref}}$

The pressure p becomes $\dfrac{\rho T}{\gamma k_0^2}$.

Here $T_{\text{ref}} = 300\,\text{K}$, $R = 287 \frac{\text{J}}{\text{Kg K}}$, $\rho_{\text{ref}} = 1.225\,\text{kg/m}^3$, $k_0 = 1.5$. In the above, the reference quantities, quantities with a tilde and specific gas constant R are dimensional. Other quantities are dimensionless.

2.1 Governing equations

Two dimensional time dependent equations for viscous, heat-conducting flow in axisymmetric form are given below. We have intentionally avoided more compact representation for the benefit of programmers.

Continuity equation:

$$\frac{\partial \rho}{\partial t} + \frac{\partial}{\partial x}(\rho u) + \frac{\partial}{\partial y}(\rho v) + \frac{\rho v}{y} = 0 \tag{1}$$

x and y momentum equations:

$$\begin{aligned}
&\frac{\partial}{\partial t}(\rho u) + \frac{\partial}{\partial x}\left(\rho u^2 + p\right) + \frac{\partial}{\partial y}(\rho u v) \\
&= \frac{\partial}{\partial x}\left[\frac{2\mu}{3}\left(2\frac{\partial u}{\partial x} - \frac{\partial v}{\partial y} - \frac{v}{y}\right)\right] \\
&\quad + \frac{\partial}{\partial y}\left[\mu\left(\frac{\partial v}{\partial x} + \frac{\partial u}{\partial y}\right)\right] + \frac{\mu}{y}\left(\frac{\partial v}{\partial x} + \frac{\partial u}{\partial y}\right) - \frac{\rho u v}{y}
\end{aligned} \tag{2}$$

$$\begin{aligned}
&\frac{\partial}{\partial t}(\rho v) + \frac{\partial}{\partial x}(\rho u v) + \frac{\partial}{\partial y}\left(\rho v^2 + p\right) \\
&= \frac{\partial}{\partial x}\left[\mu\left(\frac{\partial v}{\partial x} + \frac{\partial u}{\partial y}\right)\right] + \frac{\partial}{\partial y}\left[\frac{2\mu}{3}\left(2\frac{\partial v}{\partial y} - \frac{v}{y} - \frac{\partial u}{\partial x}\right)\right] \\
&\quad - \frac{\rho v^2}{y} + \frac{2\mu}{3y}\left(2\frac{\partial v}{\partial y} - \frac{v}{y} - \frac{\partial u}{\partial x}\right) \\
&\quad - \frac{2\mu}{3y}\left(\frac{2v}{y} - \frac{\partial u}{\partial x} - \frac{\partial v}{\partial y}\right)
\end{aligned} \tag{3}$$

Energy equation:

$$\begin{aligned}
&\frac{\partial}{\partial t}(\rho E) + \frac{\partial}{\partial x}\left[(\rho E + p)\, u\right] + \frac{\partial}{\partial y}\left[(\rho E + p)\, v\right] \\
&= \frac{\partial}{\partial x}\left(k\frac{\partial T}{\partial x}\right) + \frac{\partial}{\partial y}\left(k\frac{\partial T}{\partial y}\right) + \frac{k}{y}\frac{\partial T}{\partial y} \\
&\quad + \frac{\partial}{\partial x}\left[u\frac{2\mu}{3}\left(2\frac{\partial u}{\partial x} - \frac{\partial v}{\partial y} - \frac{v}{y}\right) + v\mu\left(\frac{\partial v}{\partial x} + \frac{\partial u}{\partial y}\right)\right] \\
&\quad + \frac{\partial}{\partial y}\left[u\mu\left(\frac{\partial v}{\partial x} + \frac{\partial u}{\partial y}\right) + v\frac{2\mu}{3}\left(2\frac{\partial v}{\partial y} - \frac{v}{y} - \frac{\partial u}{\partial x}\right)\right] \\
&\quad + v\frac{2\mu}{3y}\left(2\frac{\partial v}{\partial y} - \frac{v}{y} - \frac{\partial u}{\partial x}\right) + u\frac{\mu}{y}\left(\frac{\partial v}{\partial x} + \frac{\partial u}{\partial y}\right) \\
&\quad - \frac{(\rho E + p)\, v}{y}
\end{aligned} \tag{4}$$

where $E = \frac{p}{\rho(\gamma - 1)} + \frac{1}{2}\left(u^2 + v^2\right)$.

Conservation of mass, momentum and energy equations are solved along with the state equation, $p = \frac{\rho T}{\gamma k_0^2}$ for obtaining the density, velocity, pressure and temperature field. Viscosity is calculated from Sutherland's law.

2.2 Numerical scheme

The governing equations have been solved using the AUSM+ scheme [34]. It belongs to the flux-vector splitting family of schemes and is known for its low numerical dissipation. The details of the scheme can be found in the cited reference. In our solver, we employ the MUSCL approach to interpolate variables to the cell faces for use in convective terms. Since sharp gradients are present in the form of shocks, we also apply the minmod limiter to limit the interpolated values. The solver is explicit and time stepping is performed with a four-stage Runge–Kutta time integration scheme [35]. Viscous fluxes are calculated by standard second-order accurate central differencing formulas.
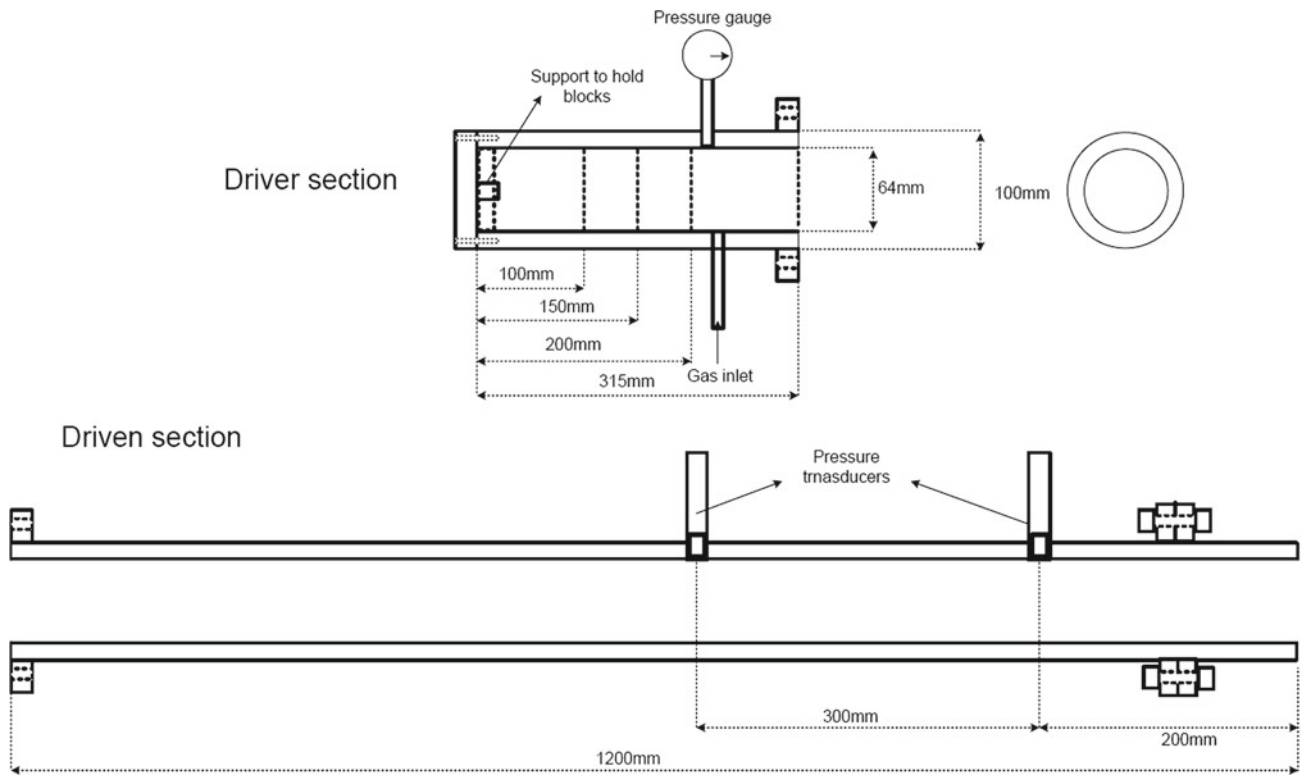
Fig. 1 Driver and driven section of the shock tube

2.3 Problem domain and discretization

Figure 1 shows the schematic of the variable driver section length shock tube. The inner and outer diameters of the shock tube are 64 and 100 mm respectively. The driven section length of the shock tube is 1,200 mm and the driver section length is kept fixed at 165 mm for the present study.

Figure 2 shows the computational domain of the problem. Figure 2b shows the region near the tube exit with reduced numbers of grid lines for clarity. One half of the shock tube is considered for simulation in the present study with symmetry condition at the centre-line. Zone 1 includes both driver and driven sections of the shock tube. The grid is uniformly distributed in the y direction and stretched away from the exit along the x direction in zone 1. The grid is also stretched in zone 2 and zone 3 away from the shock tube exit.

2.4 Initial and boundary conditions

The simulation is initialized everywhere with ambient conditions (pressure at 1.01325 bar with a temperature of 300 K) except at the driver section, where the pressure is several times (3 and 7 in the studies presented here) the ambient value while the temperature does not vary. No-slip conditions are applied at left closed end of the shock tube and also at the
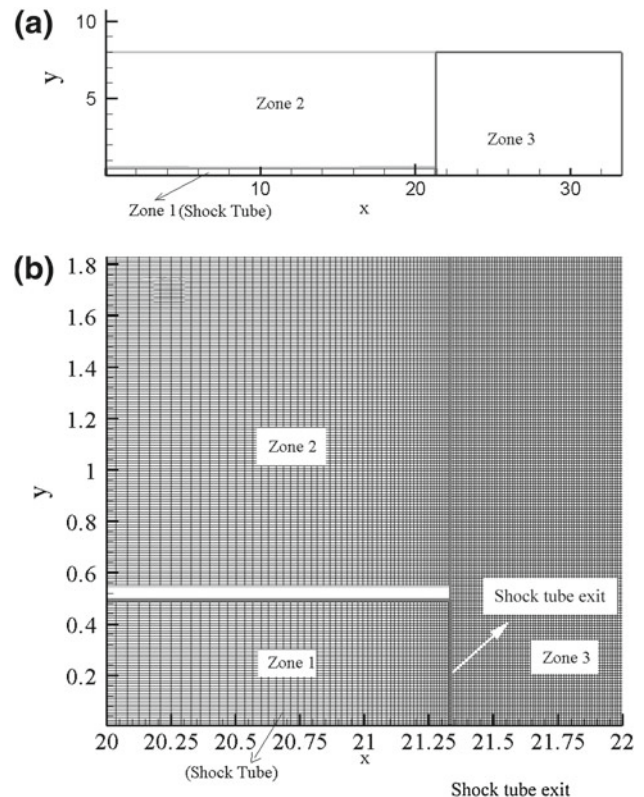

Fig. 2 Shock tube and discretization domain

outer walls of it (the top horizontal part and a few cells thick vertical part at the right end). The remaining open boundaries at the top, left and right edges of the domain are treated by the NSCBC boundary condition of Poinsot and Lele [36]. In this form, the basic idea is to solve the governing equations guided by a characteristic decomposition. The equations are reorganized and terms corresponding to waves propagating in the direction normal to the boundary are expressed using amplitudes of characteristic waves. This approach leads to much reduced reflection of waves from the open boundaries compared to simple extrapolation of variables.

3 Experimental setup and description

Figure 3 shows the schematic and the detailed instrumentation of the experimental setup. The compressible vortex ring generated at the open ended shock tube is captured using a CCD camera and laser sheet. Mylar sheets of different thicknesses are used as diaphragm and it is ruptured using a pneumatic plunger. Three PCB pressure transducers PT1, PT2 and PT3 are placed inside the tube for measuring the shock speed. The signal from the pressure transducers is acquired at a sampling rate of 100 kSa/s using NI 4472, 24-bit sound and vibration DAQ (Data Acquisition) card. The shock speed is calculated from the time difference obtained from the sharp rise in transducer signal and the distance between the pressure transducers. The velocity field of vortex ring and the trailing jet is measured using particle image velocimetry. A double

pulsed Nd: YAG laser (200 mJ/pulse, 10 Hz) is used for illuminating the flow field. The beam is delivered from the laser head to the experimental zone by an articulated arm with a sheet forming optics at the end. The sheet forming optics consists of two spherical lenses and a cylindrical lens. The thickness of the laser sheet is approximately 1mm. The sheet is aligned to the centre line of the shock tube and cuts the radial plane. A 12 bit CCD camera of 4 MP (megapixel) resolution is used for capturing the particle images.

The voltage signal from PT2 is used for triggering the external delay generator which has a variable delay from 1 μs to 10 ms. This is used for synchronizing the laser sheet and CCD camera. In every experiment, only one double shutter image capturing the flow field is obtained. The flow field at different times is captured by adjusting the delay in the delay generator. PIV measurements are carried out in dark conditions. The time between the two laser pulses is 3 to 5 μs for these high speed measurements. Time between the pulses is chosen in such a way that the maximum displacement of the particles within the interrogation window is less than or equal to 25% of the interrogation window length. The total area of the captured images is 150 mm × 150 mm. The maximum displacement is obtained theoretically from induced velocity behind the shock wave. Fog is used as seeding particle in all experiments. The particles have a diameter and density of 1 μm and 1.353 kg/m^3.

The driven section is filled with fog prior to the bursting of diaphragm. Stokes' number [37] which shows the ratio of the particle relaxation time to the characteristic time scale of the fluid has been calculated to find the response of seed
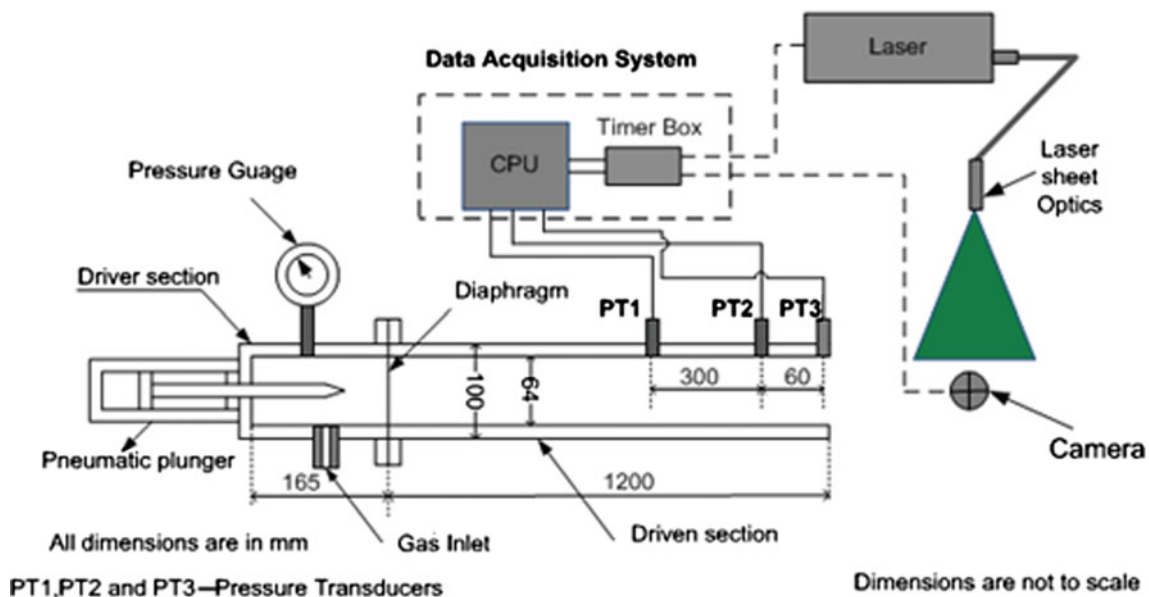

Fig. 3 Schematic of the experimental setup

particles to high velocity gradients and how well they follow the fluid. Stokes' number calculated by taking the inner diameter of the shock tube and velocity behind the incident shock shows that the value is very small compared to unity. This shows that seed particles can respond very well to the high velocity gradients of the flow. Dynamic Studio software of Dantec Dynamics is used for acquisition and analysis of the captured particle images. Analysis is carried out with interrogation window of size 32×32 pixels and an adaptive correlation with a 50% overlap.

The shock speed cannot remain same throughout the shock tube length due to shock formation process, boundary layer development, and uneven bursting of diaphragm. The modeling with inviscid assumption showed good agreement with experimental results after shock formation. A number of investigators [38–40] showed that calculations based on ideal model of shock tube flow (i.e. no attenuation, instantaneous diaphragm removal, and one-dimensional flow) agreed satisfactorily with experiment. The observed shock was slightly weaker than the predicted shock for the given initial conditions. However, the shock speed inside the tube varied significantly during initial stage for different experiments due to nonuniformity in diaphragm rupturing.

The diaphragm rupture involves formation of a small opening at the centre followed by the outward tearing of the diaphragm material and its folding back process. The effective cross sectional area of the shock tube at the diaphragm location increases gradually with time compared to the ideal analysis where the maximum value is attained instantaneously. The effective velocity pushing on the driven gas increases with the degree of diaphragm opening. The opening of the diaphragm generates a train of compression waves which combine together to form a shock wave as each positive increment in the velocity sends out a compression wave. The shock tube starting process can occupy a significant portion of the shock tube length. The shock was found to be accelerating even at 40 ft [40] from the diaphragm for large diaphragm pressure ratios $\sim 10^6$.

The one-dimensional analysis and experimental studies of Alpher and White [41] predicted shock enhancement due to change in area at the diaphragm, even for larger diaphragm pressure ratios. However, the acceleration in shock speed was observed for long driver section length. The shock speed may remain constant or decelerate towards the shock tube end for smaller driver section shock tube based on diaphragm rupture [18] and driven section length. In the present study, small driver section (165 mm) and long driven section (1,200 mm) shock tube is used as the unsteady evolution of compressible vortex ring and trailing jet are the main objective of the study. The maximum reduction in shock speed of 1.75% is observed between PT1 and PT3 for PR = 3 and it is 1.4% for PR = 7. The consistency in shock speed is calculated by performing 30 experiments for given pressure. The shock

Mach number calculated from the experiments may have the maximum variation of around 4%.

4 Results and discussion

Flow visualizations are performed with time difference of 40 μs using laser sheet and CCD camera for measuring the translational velocity and the diameter of the vortex ring. Translational velocity is calculated using the locations of vortex centre and the time difference (40 μs). The vortex core centre is calculated from flow visualization data. In numerical simulation it has been calculated by searching for maximum vorticity within an estimated area where the vortex core is located. For $M = 1.57$, the vortex ring is highly stretched and distorted and hence its translational velocity may have $\pm 5\%$ variation. For $M = 1.36$, this variation is considerably less.

4.1 Evolution of vortex ring for PR = 3

Figure 4 shows the evolution of starting jet and the vortex ring for PR = 3 and $M = 1.36$. The pressure ratio across the incident shock at shock tube exit is 1.75. The flow is adjusted to the ambient condition via propagation of disturbance waves (sound waves) into the shock tube. The flow expands like a subsonic jet at the exit as the pressure ratio is less than the critical pressure to reach sonic condition. It has also been observed experimentally and numerically that the jet exhausted from the open end tend to be subsonic jet for PR < 4.1 [33]. It is confirmed from numerical shadowgraph in Fig. 4b–h that no shock cell structure and significant density variation in the trailing jet is observed. Figure 4a shows the velocity and vorticity distribution during the vortex ring formation at $t = 360$ μs (measured from the time the shock was at exit of the tube). Here the flow at the exit expands to reach the ambient condition by subsonic expansion. Figure 4b shows the numerical shadowgraph obtained at $t = 360$ μs and it shows the density variation in the flow field. Large density gradient is observed across the incident shock and the strength of the incident shock is more along the axis and it reduces continuously away from the axis due to planar nature of the shock which has been closely matched with experimental results [18]. Significant density variations are also observed at the boundary of the vortex core and free shear layer of trailing jet. The vortex ring is virtually unaffected by the trailing jet as the flow expands like subsonic jets.

Figure 4c shows the vortex ring at $t = 760$ μs during which the jet boundary shrinks inwards (Fig. 4c, d) and this shows the reduction of trailing jet velocity compared to the vortex ring translational velocity. The jet velocity at the exit is also less compared to the velocity near the ring. The strength of the incident shock (Fig. 4d) is reduced significantly as compared to shock at $t = 360$ μs. The velocity vectors near the ring are

Fig. 4 Vorticity field and numerical shadowgraph of vortex ring during evolution for $M = 1.36$ at $t = 360\,\mu\text{s}$ (**a**, **b**), $760\,\mu\text{s}$ (**c**, **d**), $1360\,\mu\text{s}$ (**e**, **f**), and $3{,}360\,\mu\text{s}$ (**g**, **h**)
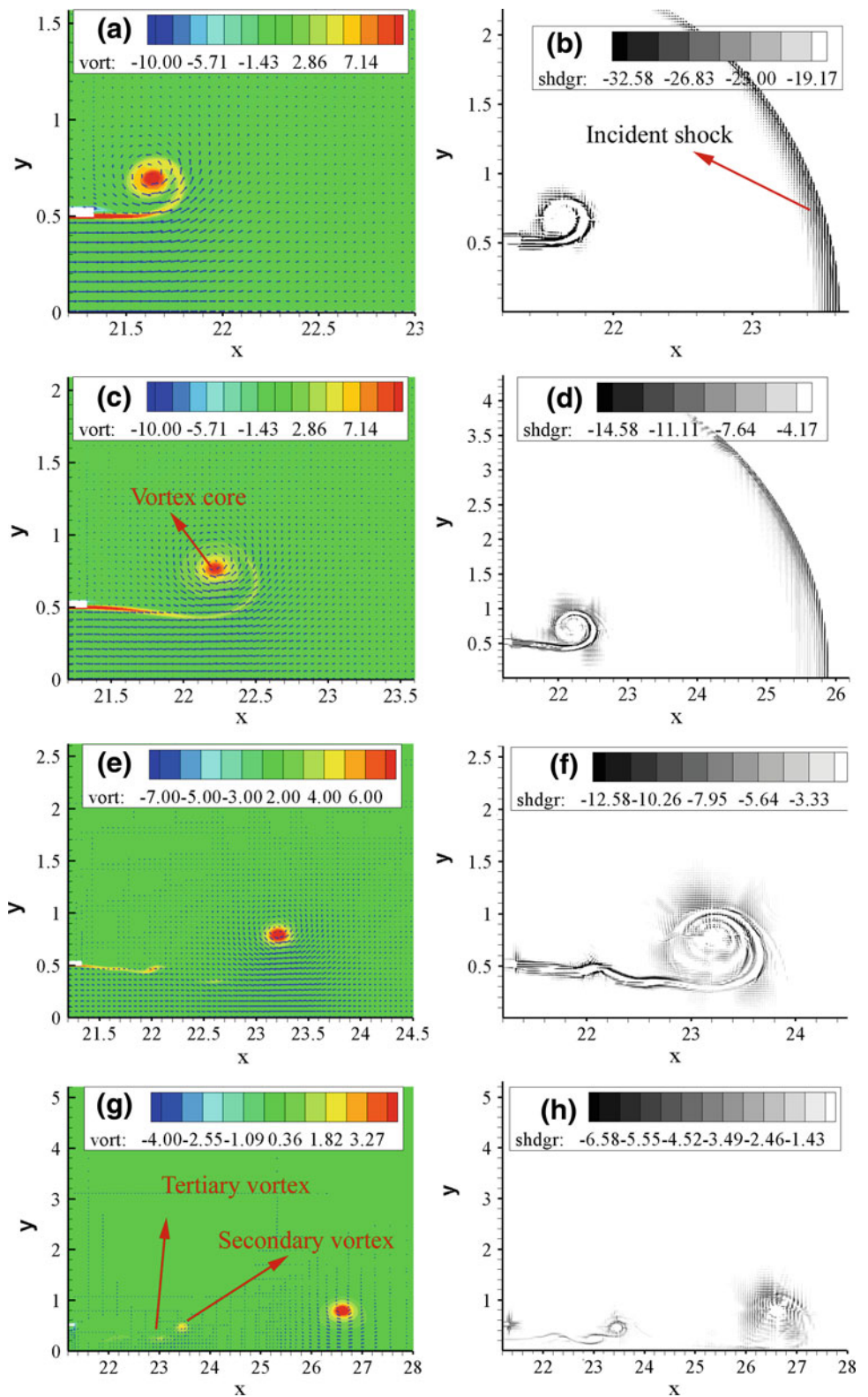
much higher compared to the trailing jet and exit velocities in Fig. 4e ($t = 1{,}360\,\mu\text{s}$). The primary vortex ring is pinched off from the trailing jet at this time and translates along the downstream direction. Secondary and tertiary vortices grow

significantly as the primary vortex ring pinches off which is seen from Fig. 4g, h. The self induced velocity of the vortex ring reduces gradually due to viscosity during vortex ring translation. Vortex ring translates very long distance before

Fig. 5 Vorticity field and
numerical shadowgraph of
vortex ring during evolution for
$M = 1.57$ at $t = 240\,\mu s$ (**a**, **b**),
640 μs (**c**, **d**), 920 μs (**e**, **f**), and
1,600 μs (**g**, **h**)
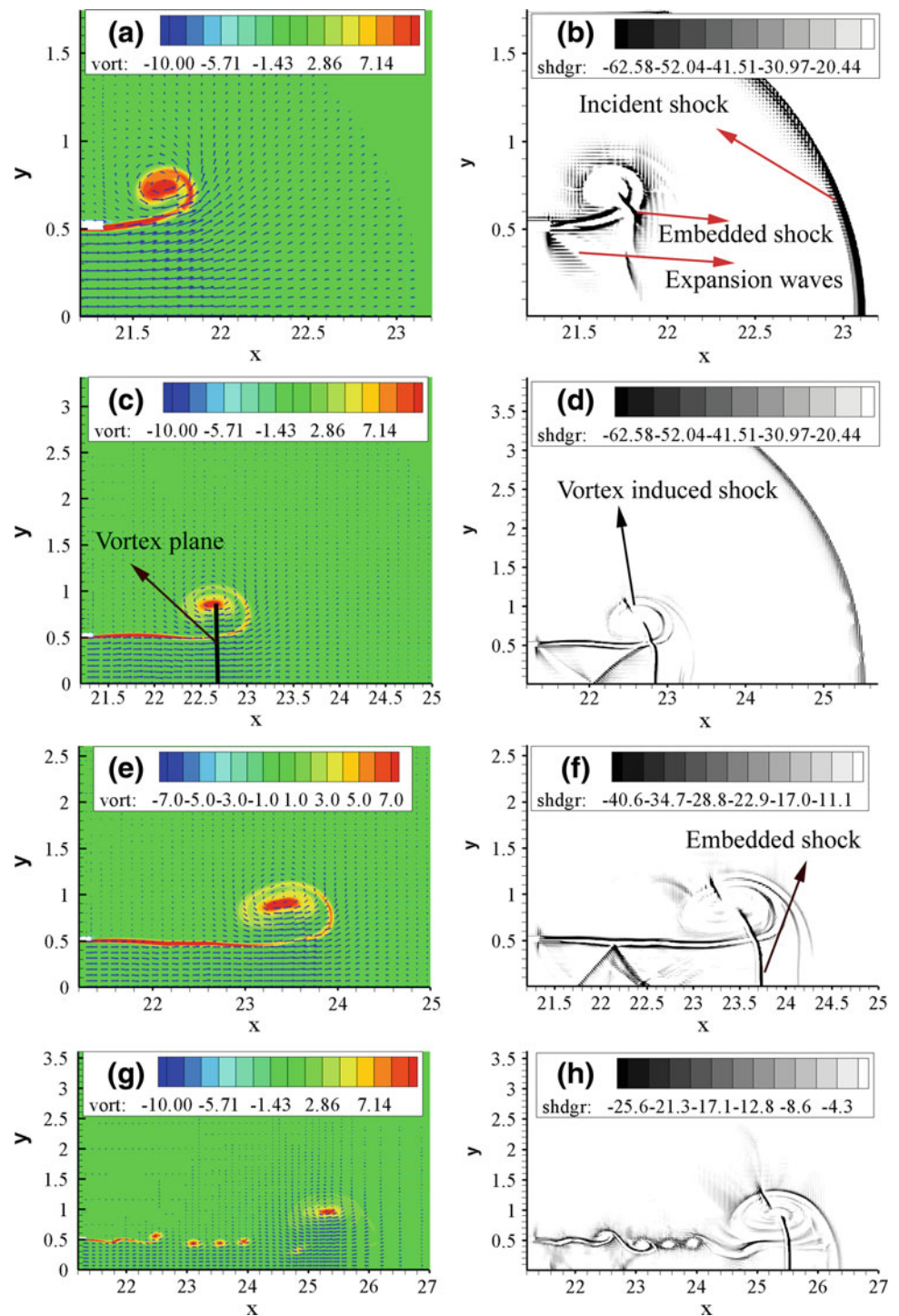
it diffuses in the atmosphere due to Widnall instability [42].
Figure 4g, h show the vortex ring at $t = 3{,}360\,\mu s$ and still
the vortex ring maintains its compact nature.

4.2 Evolution of vortex ring for PR = 7

Figure 5 shows the evolution of impulsive jet and compress-
ible vortex ring for PR = 7 ($M = 1.57$). The pressure ratio

across the incident shock at shock tube exit is 2.52. The dis-
turbance waves continuously propagate inside the shock tube
until the flow reaches sonic condition. Here the flow at the exit
exhibits sonic under expanded jet condition as the pressure
ratio is more than 1.89. The flow accelerates rapidly at the
exit as the supersonic expansion takes place which is seen in
Fig. 5a, b at $t = 240\,\mu s$. The embedded shock near the vortex
is also clearly identified in Fig. 5b. Figure 5a shows the roll

up and formation of vortex ring. The supersonic expansion of the flow significantly affects the formation of vortex ring as compared to $M = 1.36$ and the vortex ring is stretched during formation. Figure 5c, d at $t = 640 \, \mu s$ show translation of the vortex ring along with the trailing jet. The shock cell structure formed in the axial region is similar to the structure obtained from differential interferometry [11] and high-speed schlieren photography [20].

Strong velocity gradient ahead of the vortex plane in Figs. 5c and 8a shows the existence of embedded shock which is verified from numerical shadowgraph in Fig. 5d. Vortex induced shock [33] is also identified in Fig. 5d. However it is not seen in Fig. 5c from velocity and vorticity as the strength is less compared to the embedded shock. The primary vortex ring is highly stretched and deformed due to the presence of strong trailing jet, embedded and vortex induced shocks. Both embedded and vortex induced shocks terminate near the vortex core due to strong viscous effects [11].

Figure 5f shows the numerical shadowgraph obtained when the primary vortex ring pinches off from the trailing jet at $t = 920 \, \mu s$ which is seen in Fig. 5e. As the expansion waves disappear near the exit, the trailing jet strength decreases (Fig. 5f, h) and subsequently the strength of the embedded shock also decreases. However the embedded shock and vortex induced shocks are present in the flow field. They lose their strength gradually and finally disappear due to viscous dissipation. The shear layer vortices formed at the trailing jet due to Kelvin–Helmholtz instability grow faster after the primary vortex ring pinches off and form secondary and tertiary vortex rings which are seen in Fig. 5g, h at $t = 1,600 \, \mu s$.

Figure 6 shows the iso-pressure and density contours for PR $= 3$ and 7 at $t = 1,040 \, \mu s$ and $t = 640 \, \mu s$ where the vortex ring is approximately at same distance from the shock tube exit. Figure 7 shows the flow visualization pictures obtained exactly at the same time for PR $= 3$ and 7. The vortex core is compact and is not affected by the trailing jet
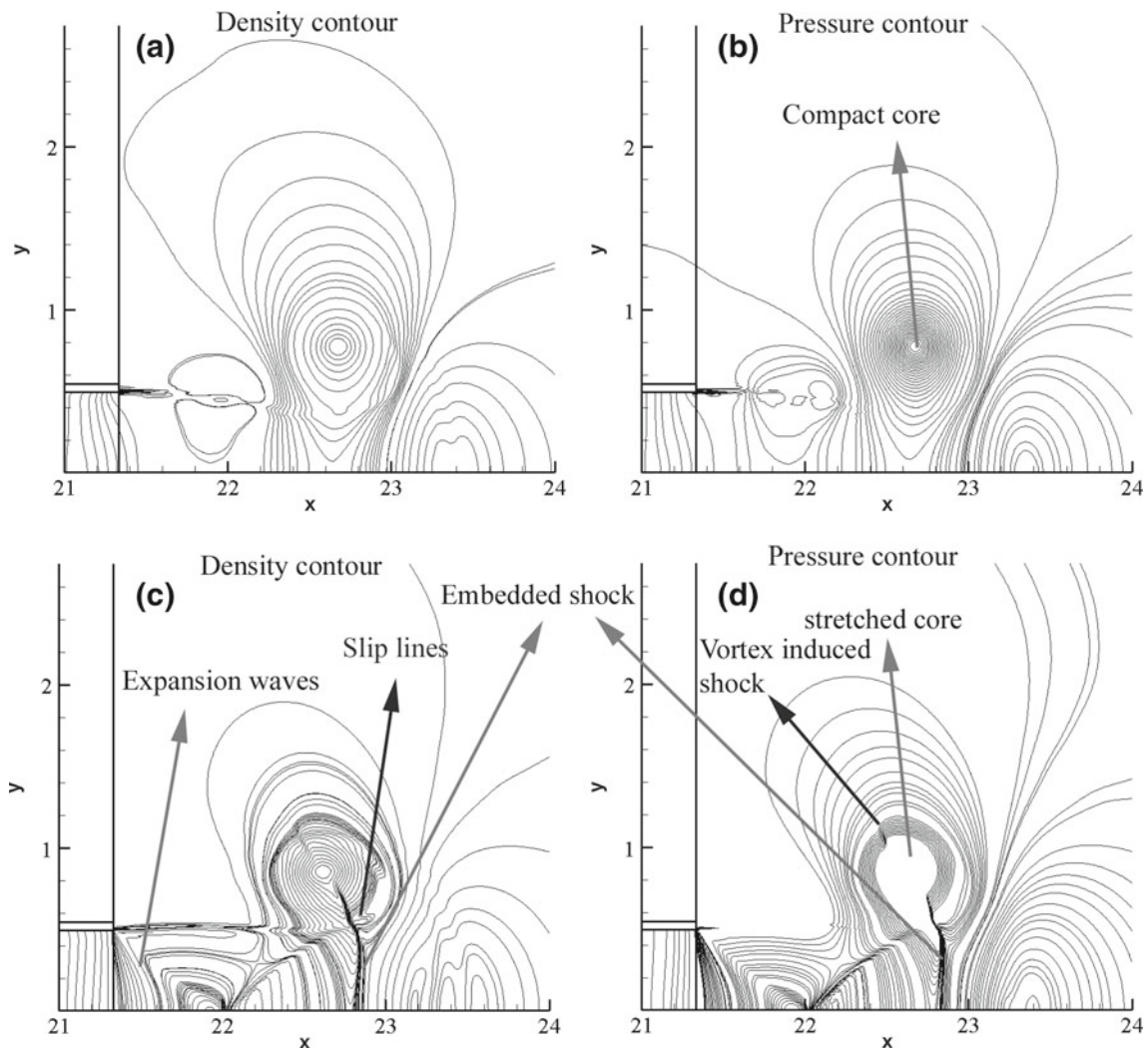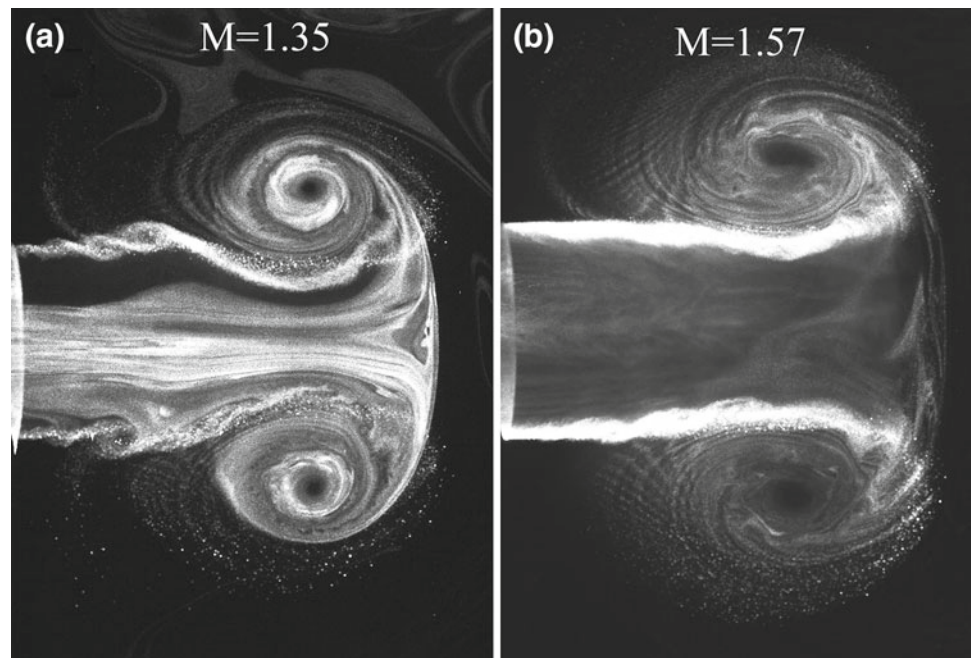

Fig. 6 Iso-pressure and density contours at $t = 1,040 \, \mu s$ (**a**, **b**) and 640 μs (**c**, **d**) for PR $= 3$ and 7

Fig. 7 Flow visualization of vortex ring at **a** $t = 1{,}040\,\mu$s and **b** 640 μs for PR = 3 and 7

for PR = 3 and it is seen in the density and pressure contours in Fig. 6a, b. The changes in the flow field are more gradual as the flow expands subsonically. The shear layer vortices are also observed from both flow visualization and contour plots. Figure 6c, d show the pressure and density contours for PR = 7 where shock cell structure and embedded shock makes the flow more complicated. The vortex core is severely affected for PR = 7 though shock/expansion waves are not observed in Fig. 7b. The existence of embedded shock, vortex induced shock and slip lines along with the strong trailing jets are responsible for stretching and deformation of the core. It is interesting to note that the vortex shape is more elliptical at higher pressure ratio. In incompressible flow orientation of the vorticity gradient vector with respect to the principal strain axes is linked to such gradient tilting. To what extent similar arguments can be associated with the elliptic shape of the vortex in the present case hasn't been explored here but will be studied in future.

4.3 Comparison of numerical results with experiment

In this section, results obtained from numerical simulation are compared with PIV results. Unlike simulation, the *M* calculated from experiments may not be same (maximum variation around 4%) for same PR due to uneven bursting of diaphragm.

4.3.1 Comparison of velocity field

Figure 8 shows the velocity field obtained from simulation and PIV measurements. Figure 8a, b show velocity field for PR = 7 at $t = 600\,\mu$s. The velocity field is presented by

taking the mirror image for showing the shock cell structure and the embedded shock as the simulation is performed for one half of the tube. The nature of the shock/expansion wave structure and the presence of embedded shock are identified in simulation (Fig. 8a) from velocity variations. However only the embedded shock is clearly identified from PIV results and the trailing jet velocity is less compared to simulation. This is due to the small rupturing area of diaphragm in experiments as compared to simulation where the entire diaphragm is removed simultaneously. Figure 8c, d show the results obtained for PR = 3 at $t = 640\,\mu$s. In both cases, the trailing jet exhibits subsonic flow expansion condition which is seen from the magnitude of velocity. The experimental velocities are slightly large as compared to the simulation due to slightly higher M. The vortex cores are circular and compact in Fig. 8c, d for PR = 3 whereas the vortex cores are stretched for PR = 7 in Fig. 8a, b. Figure 9 shows the velocity field of the vortex ring for PR = 3 and 7. In one half the PIV data are presented and the other half shows simulation results. Though both results matched well, the vortex ring's core vorticity and embedded shock are resolved much better in simulation as compared to the PIV.

4.3.2 Translational velocity of vortex ring

Figure 10 shows the nondimensional translational velocities obtained for PR = 3 and 7 from experiments and simulation. U_b is velocity behind the incident shock at the exit which is calculated using PIV measurement for experimental data. Translational velocity for simulation is calculated
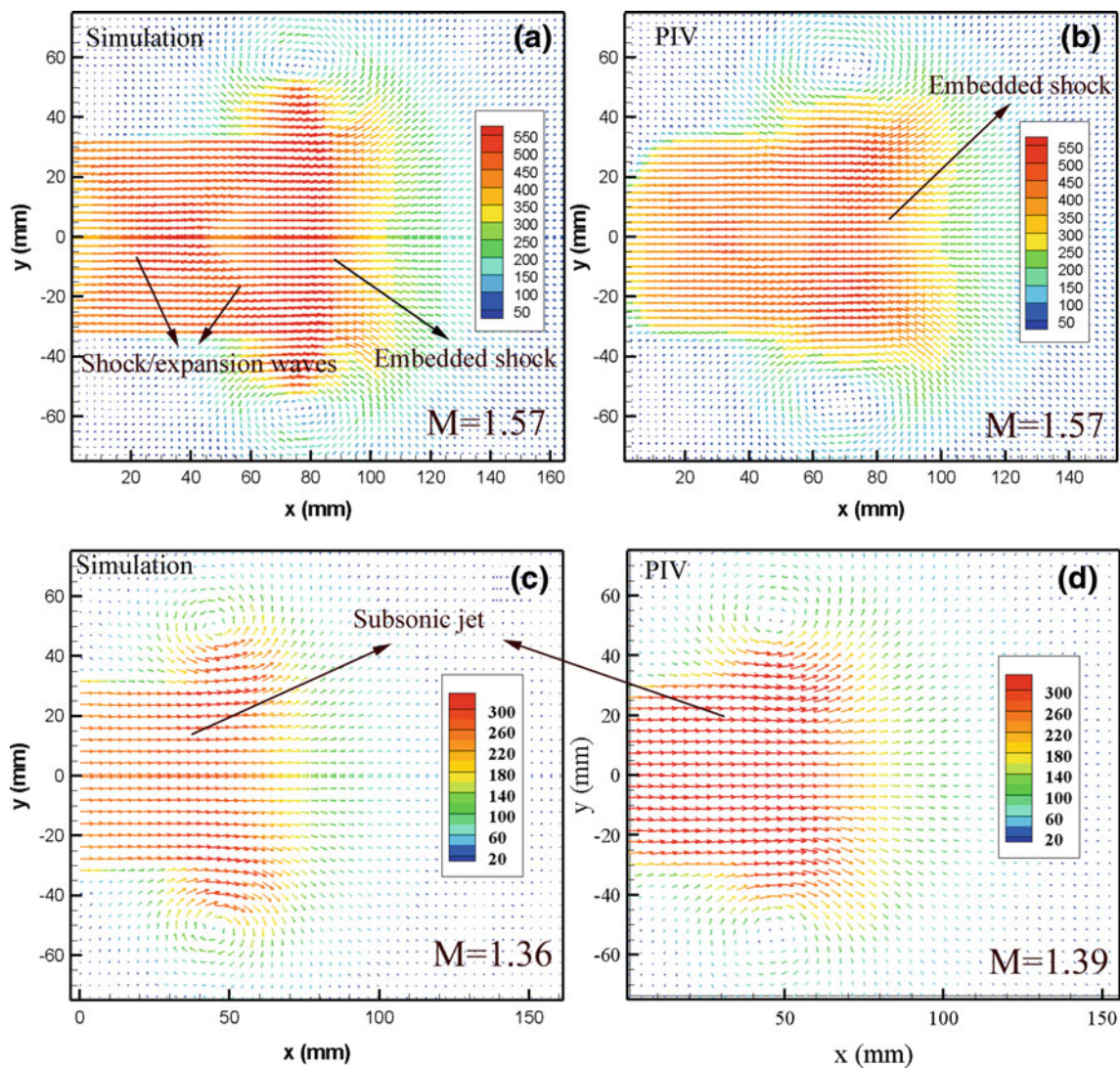
Fig. 8 Comparison of simulation and PIV results at $t = 600\,\mu s$ (**a, b**) and $t = 640\,\mu s$ (**c, d**) for PR = 7 and 3

using the distance between the centers of core vorticity whereas for experiments, it is calculated manually from flow visualization pictures obtained at 40 μs. The core of the vortex ring is elliptical in nature and it becomes more stretched as M increases. The large variation in translational velocity with time is due to the elliptical nature of the vortex core. The translational velocity increases rapidly during the initial stage of vortex ring formation. It gradually reaches to an asymptotic value during the vortex ring growth. The vortex ring translates along the downstream with its self induced velocity after it pinches off from the trailing jet. The variations of translational velocity with M and driver section length are studied extensively in Murugan and Das [17, 18]. For PR = 3, the translational velocity is notably accurate as the trailing jet does not affect the vortex ring whereas at PR = 7, it may have maximum of 10% variation due to stretching and deformation of elliptical vortex core.

4.3.3 Axial velocity of trailing jet

Figure 11 shows the nondimensional centerline velocity obtained for PR = 7 at $t = 560\,\mu s$ from both experiments and numerical simulation. The velocity along the axis increases up to 40 mm from the exit due to supersonic expansion of the flow at the exit. It gradually reduces up to 56 mm due to the presence of shock cell structure. The maximum nondimensional centerline velocity variation of 1.36 is obtained at the axial distance of 56 mm where the shock cell intercepts the axis. The velocity then gradually increases up to 75 mm where the embedded shock exists. The velocity ahead of the embedded shock reduces gradually and reaches the condition behind the incident shock. It is clear from Fig. 11 that the prediction of velocity behind the shock cell structure and the embedded shock by PIV deviate significantly from the simulation result. This is due to the accumu-
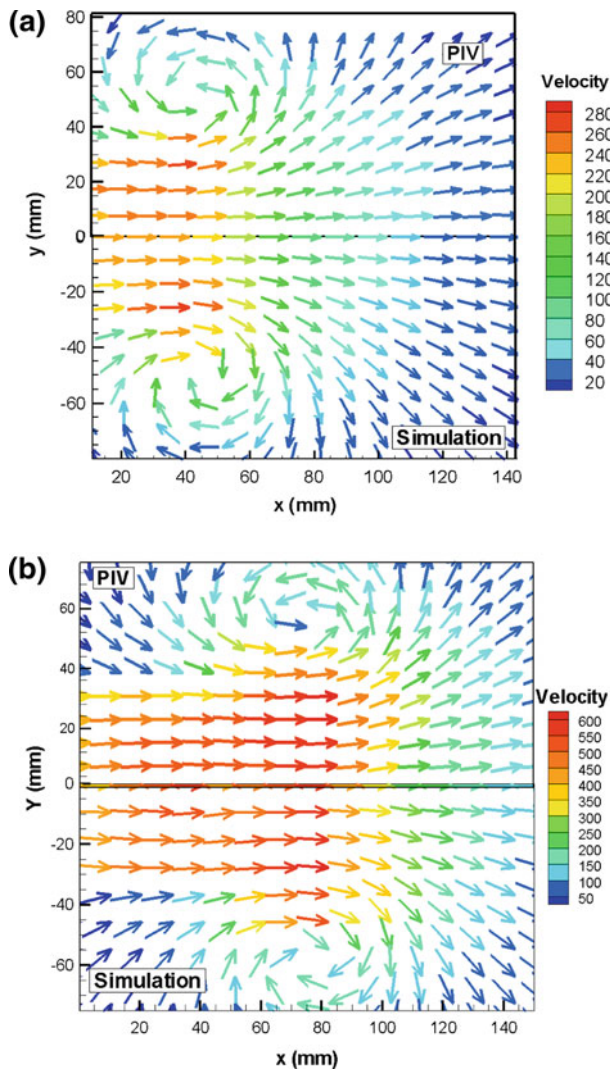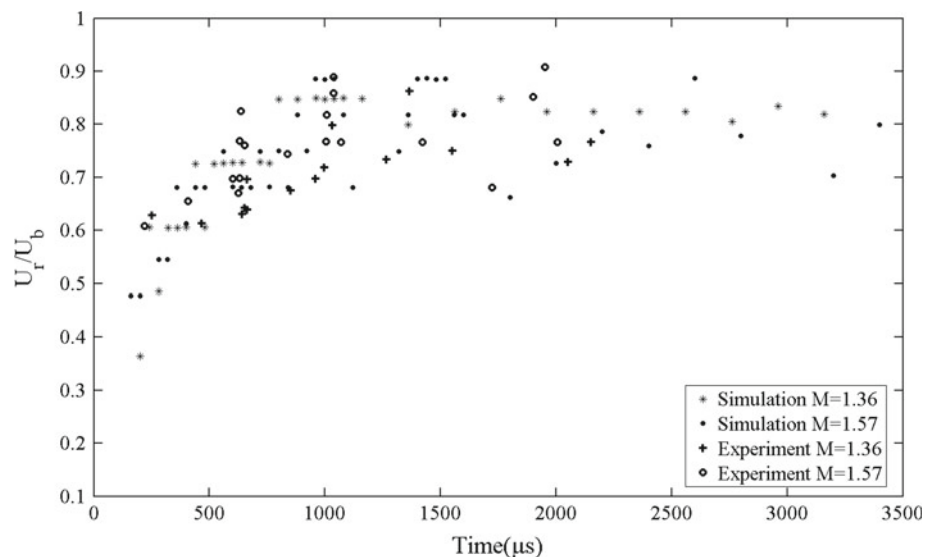
Fig. 9 Comparison of simulation and PIV results for **a** PR = 3 (t = 640 μs) and **b** PR = 7 (t = 600 μs)

lation of large number of seeding particles behind the shock. However both experiment and simulation have followed the same trend.

The lateral velocity variation across the vortex core at the mid plane of the vortex along the axial direction is plotted in Fig. 12 to predict the strength of the primary vortex. The agreement is excellent except at the edges of the vortex core. A sharp reduction in velocity at around $x = 50$ mm is observed in the simulation. It is due to the presence of vortex induced shock (Fig. 5d) at the outside portion of vortex ring. Simulation result is also start deviating from experimental results at around $x = 70$ mm. This discrepancy is likely to be the result of not capturing the shear layer vortices well at this stage of evolution in simulation, as indicated in Fig. 13. Hence, the simulation have the higher velocity compared to the experimental result. Another sharp change from $x = 80$–95 mm in simulation is due to the presence embedded shock without any trailing jet vortices. Also, the strength of the trailing jet and the embedded shock is slightly higher compared to the experiments due to complete removal of diaphragm in simulation. This may also contribute to the observed higher velocity gradient in simulation.

5 Conclusion

Formation and translation of compressible vortex ring along with the evolution of trailing jet from the open end of a shock tube have been simulated and verified with experimental results for two pressure ratios (PR) between driver and driven sections. The present study identifies the evolution of shock/expansion waves and embedded shock and their influence on deformation of the main vortex for PR = 7. The primary vortex undergoes severe stretching and deformation

Fig. 10 Variation of translational velocity of the vortex ring

Fig. 11 Centerline velocity variation of trailing jet for PR = 7 at $t = 560\mu$s
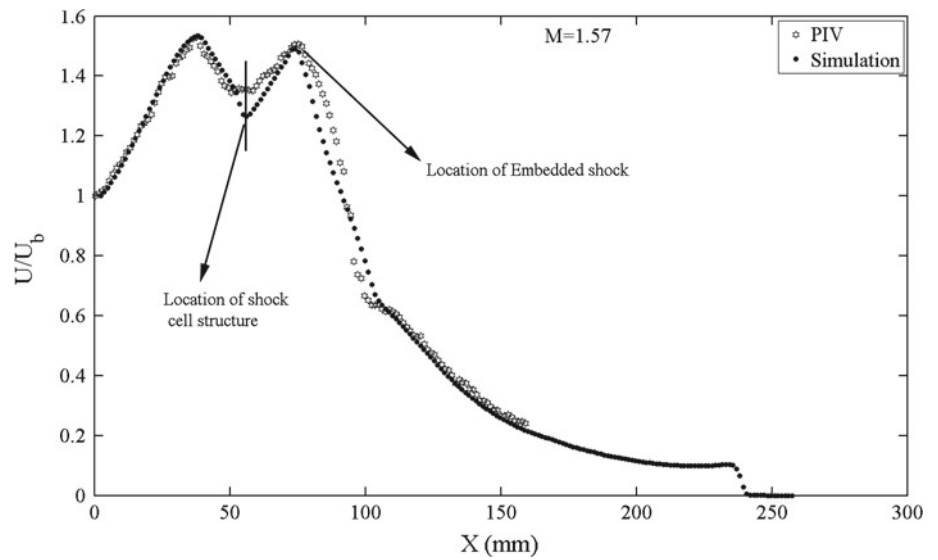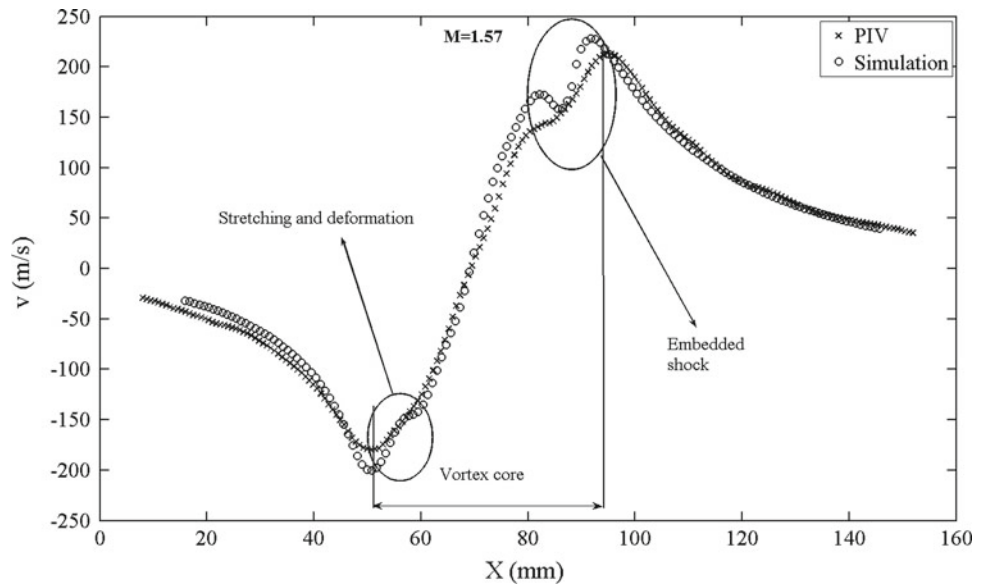

Fig. 12 Variation of lateral velocity across the vortex for PR = 7 at $t = 560\,\mu$s

due to the supersonic expansion and subsequent shock cell formation. The vortex induced shock also plays a significant role on vortex stretching and deformation. However, the vortex ring generated for PR = 3 is virtually unaffected by the subsonic jet and remains shock free during evolution. The velocity across the primary vortex and the centre line velocity of jet calculated from simulation match closely with the PIV results except behind the embedded shock and shock cell structure.

After the primary vortex ring pinches off, shear layer vortices formed at the trailing jet are distinctly visible in both simulation and experiments. However, the shear layer vortices formed during initial stage are not predicted well with present simulation. Experimental observation shows the shear layer vortices formation at the trailing jet and its entrainment into the main vortex for PR = 7. Presented comparisons give us an idea about the grid resolution and accuracy of numerical schemes needed if one desires to predict such complex flow patterns with greater accuracy. In future work, complete three-dimensional simulation of the shock tube and the compressible vortex ring will also be undertaken to study the effect of azimuthal instabilities.
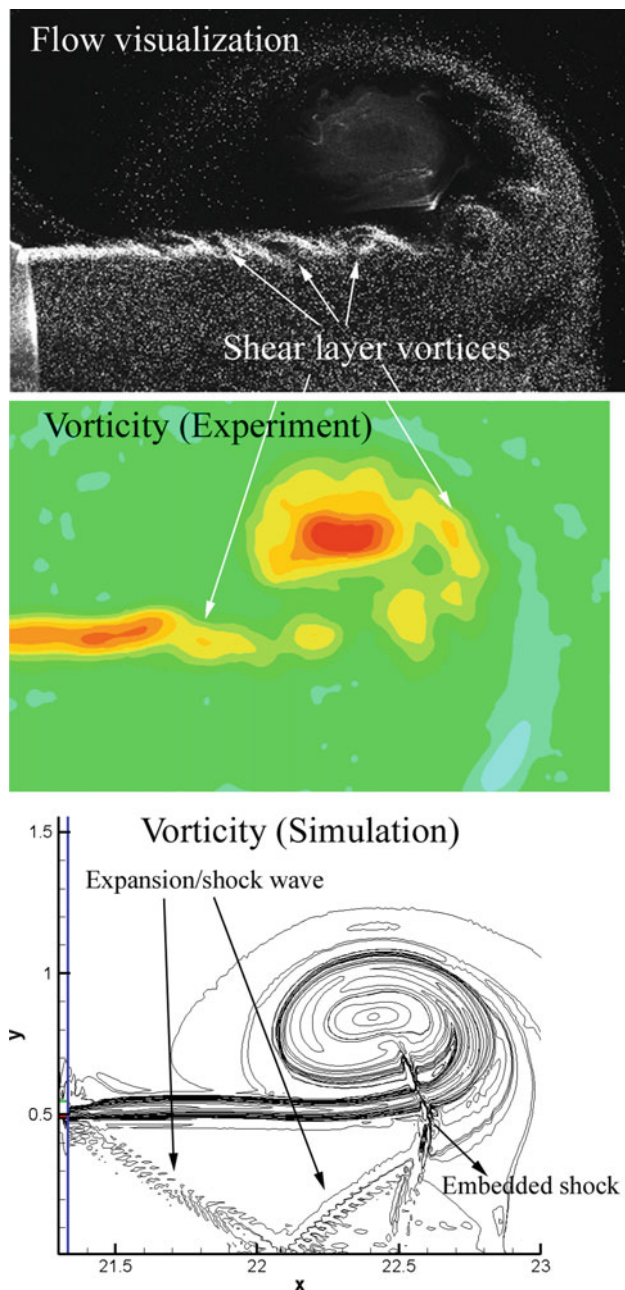
Fig. 13 Flow visualization and computed vorticity for PR = 7 at $t = 560\,\mu s$

References

1. Abate, G., Shyy, W.: Dynamic structure of confined shocks undergoing sudden expansion. Prog. Aerosp. Sci. **38**, 23–42 (2002)
2. Jiang, Z., Takayama, K., Babinsky, H., Meguro, T.: Transient shock wave flows in tubes with sudden change in cross section. Shock Waves **7**, 151–162 (1997)
3. Sun, M., Takayama, K.: Vorticity production in shock diffraction. J. Fluid Mech. **478**, 237–256 (2003)
4. Sun, M., Takayama, K.: A note on numerical simulation of vortical structures in shock diffraction. Shock Waves **13**, 25–32 (2003)
5. Maxworthy, T.: Turbulent vortex ring. J. Fluid Mech. **64**, 227–239 (1974)
6. Gharib, M., Rambod, E., Shariff, K.: A universal time scale for vortex ring formation. J. Fluid Mech. **360**, 121–140 (1998)
7. James, S., Madnia, C.K.: Direct numerical simulation of a laminar vortex ring. Phys. Fluids **8**, 2400 (1996)
8. Danaila, I., Hélie, J.: Numerical simulation of the post formation evolution of a laminar vortex ring. Phys. Fluids **20**, 073602 (2008)
9. Elder, F.K., Hass, N.: Experimental study of the formation of a vortex ring at the open end of a cylindrical shock tube. J. Appl. Phys. **23**, 1065–1069 (1952)
10. Phan, K.C., Stollery, J.L.: The effect of suppressors and muzzle brakes on shock wave strength. In: Proceedings of the 14th international symposium on shock tubes and waves, August 19–22, Sydney (1984)
11. Baird, J.P.: Supersonic vortex rings. Proc. R. Soc. Lond. Ser. A **409**, 59–65 (1987)
12. Brouillette, M., Hebert, C.: Propagation and interaction of shock-generated vortices. Fluid Dyn. Res. **21**, 159–169 (1997)
13. Arakeri, J.H., Das, D., Krothapalli, A., Lourenco, L.: Vortex ring formation at the open end of a shock tube: a PIV study. Phys. Fluids **30**, 1008–1019 (2004)
14. Murugan, T., Das, D.: Propagation and wall interaction of compressible vortex ring: qualitative study. In: The 9th Asian symposium on visualization, June 4–9, Hong Kong (2007)
15. Murugan, T., Das, D.: Structure and acoustic characteristics of supersonic vortex rings. In: FLUCOME 2007 (9th international symposium on fluid control, measurement and visualization), September 16–19, Tallahassee (2007)
16. Murugan, T., Das, D.: On evolution and acoustic characteristics of compressible vortex ring. Int. J. Aeroacoust. **7**, 199–222 (2008)
17. Murugan, T., Das, D.: Characteristics of noise produced during impingement of a compressible vortex ring on a wall. Int. J. Aeroacoust. **9**(6), 849–858 (2010)
18. Murugan, T.: Flow and acoustic characteristics of high mach number vortex rings during evolution and wall-interaction: an experimental investigation, Ph.D. Thesis, Indian Institute of Technology, Kanpur (2008)
19. Murugan, T., Das, D.: Characteristics of counter-rotating vortex rings formed ahead of a compressible vortex ring. Exp. Fluids **49**, 1247–1261 (2010)
20. Kontis, K., An, R., Edwards, J.A.: Compressible vortex-ring studies with a number of generic body configurations. AIAA **44**, 2962–2978 (2006)
21. Kontis, K., An, R., Zare-Behtash, H., Kounadis, D.: Head-on collision of shock wave induced vortices with solid and perforated walls. Phys. Fluids **20**, 016104 (2008)
22. Zare-Behtash, H., Kontis, K., Gongora-Orozco, N.: Experimental investigation of compressible vortex loops. Phys. Fluids **20**, 126105 (2008)
23. Zare-Behtash, H., Gongora-Orozco, N., Kontis, K.: Global visualization and quantification of compressible vortex loops. J. Vis. **12**(3), 233–240 (2009)
24. Zare-Behtash, H., Kontis, K., Gongora-Orozco, N., Takayama, K.: Compressible vortex loop: effect of nozzle geometry. Int. J. Heat Fluid Flow **30**, 561–576 (2009)
25. Zare-Behtash, H., Kontis, K., Gongora-Orozco, N., Takayama, K.: Shock wave induced vortex loops emanating from nozzles with singular corners. Exp. Fluids **49**, 1005–1019 (2010)
26. Bussing, T., Pappas, G.: An introduction to pulse detonation engines. In: 32nd aerospace sciences meeting and exhibit, AIAA Paper 94-0263, Reno, Jan 10–13 (1994)
27. Brun, R., Reboh, R.: Initial flow model in shock tubes. AIAA J. **15**(9), 1344–1345 (1977)
28. Mirels, H.: Laminar boundary layer behind shock advancing into stationary fluid, NACA TN 3401 (1955)

29. Mirels, H.: Correlation formulas for laminar shock tube boundary layer. Phys. Fluids **9**(7), 1265–1272 (1966)
30. Petersen, E.L., Hanson, R.K.: Improved turbulent boundary-layer model for shock tubes. AIAA J. **41**(7), 1314–1322 (2003)
31. Endo, M., Iwamoto, J.: Numerical analysis of pulsatile jet from exhaust pipe. JSAE Rev. **20**, 243–249 (1999)
32. Saito, T., Takayama, K.: Numerical simulations of nozzle starting process. Shock Waves **9**, 73–79 (1999)
33. Ishii, R., Fujimoto, H., Hatta, N., Umeda, Y.: Experimental and numerical analysis of circular pulse jets. J. Fluid Mech. **392**, 129–153 (1999)
34. Liou, M.-S.: A sequel to AUSM: AUSM+, 1996. J. Comput. Phys. **129**, 364–382 (1996)
35. Arnone, A., Liou, M.-S., Povinelli, L.A.: Multigrid time-accurate integration of Navier–Stokes equations. NASA TM 106373 (1993)
36. Poinsot, P.J., Lele, S.K.: Boundary conditions for direct simulations of compressible viscous flows. J. Comput. Phys. **101**, 104–129 (1992)
37. Melling, A.: Tracer particles and seeding for particle image velocimetry. Meas. Sci. Technol. **8**, 1406–1416 (1997)
38. Geiger, F.W., Mautz, C.M., Hollyer, R.N. Jr.: The shock tube as an instrument for the investigation of transonic and super-sonic flow patterns, University of Michigan, Engr. Res. Inst. Rep., Proj. M 720-4 (1949)
39. Glass, I.I., Martin, W., Patterson, G.N.: A Theoretical and experimental study of the shock tube, U.T.I.A. Report No. 2 (1953)
40. White, D.R.: Influence of diaphragm opening time on shock-tube flows. J. Fluid Mech. **4**, 585–599 (1958)
41. Alpher, R.A., White, D.R.: Flow in shock tubes with area change at the diaphragm. J. Fluid Mech. **3**, 457–470 (1958)
42. Widnall, S.E., Sullivan, J.P.: On the stability of vortex rings. Philos. Trans. R. Soc. Lond. Ser. A **332**, 335–353 (1973)